Journal of the European Ceramic Society 47 (2027) 118945

Contents lists available at ScienceDirect

Journal of the European Ceramic Society

journal homepage: www.elsevier.com/locate/jeurceramsoc

Spark plasma sintering of an innovative bioactive glass containing therapeutic ions: Densification, controlled devitrification, mechanical properties and in vitro bioactivity

Martina Tetti [a], Roberto Orrù [a,*], Giacomo Cao [a], Sebastiano Garroni [b], Simone De Micco [b], Devis Bellucci [c,1], Valeria Cannillo [c,1]

[a] Dipartimento di Ingegneria Meccanica, Chimica, e dei Materiali, Unità di Ricerca del Consorzio Interuniversitario Nazionale per la Scienza e Tecnologia dei Materiali (INSTM), Università degli Studi di Cagliari, via Marengo 2, Cagliari, 09123, Italy
[b] Dipartimento di Scienze Chimiche, Fisiche, Matematiche e Naturali, Università degli Studi di Sassari, Via Vienna 2, Sassari, 07100, Italy
[c] Dipartimento di Ingegneria "Enzo Ferrari", Università di Modena e Reggio Emilia, Via P. Vivarelli 10, Modena, 41125, Italy

ARTICLE INFO

Keywords:
Bioactive glass
Hydroxyapatite
Glass-ceramics
Spark Plasma Sintering
Mechanical Properties
Therapeutic ions

ABSTRACT

A novel Mg and Sr co-doped Bio_MS glass with a high crystallization activation energy (370 kJ/mol) was processed in this work by Spark Plasma Sintering (SPS) to achieve nearly fully dense samples. The material remains fully amorphous up to 800 °C, while higher temperatures lead to devitrification and the formation of glass-ceramics containing pseudowollastonite and wollastonite. The structural adaptability of the resulting products allows their biological and mechanical performance to be suitably tailored: lower SPS temperatures were found to maximize surface reactivity and accelerate HAp formation, whereas higher sintering temperatures improve hardness and Young's modulus. Furthermore, SPS-processed Bio_MS ensures a controlled release of therapeutic Si, Ca, Mg, and Sr ions, making it an innovative solution for bone tissue engineering.

1. Introduction

Since their discovery, Bioactive Glasses (BGs) have attracted significant attention for clinical use primarily because of their superior ability, compared to alternative bioceramics, to rapidly promote hard tissue regeneration when in contact with biological environments [1–5]. More recently, the utilization of BGs has been extended beyond the orthopedic and dental fields, also involving soft tissue areas such as angiology, oncology, drug delivery, wound healing, ophthalmology, etc. [6]. A beneficial contribution in all these contexts was provided by the possibility to introduce suitable therapeutic ions into the glass matrix, to better meet the specific needs of the biomedical applications to which BGs are addressed [7,8].

The most widely employed and investigated bioactive glass is undoubtedly the 45S5 Bioglass® developed by Larry Hench in 1969, and characterized by the composition 45% SiO_2, 24.5%Na_2O, 24.5% CaO, and 6% P_2O_5, by weight (corresponding to 46.1 SiO_2, 26.9 CaO, 24.4 Na_2O, 2.6 P_2O_5, mol%) [1]. The most critical issue associated with this glass is its relatively low crystallization temperature, near 600°C [9]. Thus, when 45S5 glass powders are sintered, the resulting bulk products are usually crystallized, so that the related bioactivity is reduced since crystalline phases are less bioactive than the original amorphous one [10]. This drawback can be in part overcome by taking advantage of efficient hot-pressing methods, like the Spark Plasma Sintering (SPS), for glass powder consolidation. Indeed, as summarized in Table 1, high relative densities, in the range 92–100%, can be achieved when 45S5 powders are processed by SPS at 500–550°C, while largely retaining the initial amorphous nature of the glass, albeit the presence of crystalline phases ($Na_2CaSi_2O_6$ or $Na_6Ca_3Si_6O_{18}$) was also generally detected [11–21].

Another complementary approach is the development of alternative bioactive glass compositions with lower tendency to crystallize compared to the 45S5 system. They include the so-called BioK (46.1 SiO_2, 26.9 CaO, 24.4 K_2O, 2.6 P_2O_5, mol%) [22,23], BG_Ca/Mix (47.2 SiO_2, 45.6 CaO, 2.3 Na_2O, 2.3 K_2O, 2.6 P_2O_5, mol%) [24] and BGMS10 (47.2 SiO_2, 25.6 CaO, 10 MgO, 10 SrO, 2.3 Na_2O, 2.3 K_2O, 2.6 P_2O_5, mol %) [25], the first two characterized by a crystallization temperature of 880°C and the latter of 932°C, thus exceeding that of standard 45S5 by

* Corresponding author.
E-mail address: roberto.orru@unica.it (R. Orrù).
[1] Last, co-last authors: contributed equally to this work.

https://doi.org/10.1016/j.jeurceramsoc.2026.118945
Received 24 June 2026; Received in revised form 4 October 2026; Accepted 6 October 2026
Available online 7 October 2026
0955-2219/© 2026 The Author(s). Published by Elsevier Ltd. This is an open access article under the CC BY license (http://creativecommons.org/licenses/by/4.0/).

more than 250 °C. As reported in Table 1, the use of the SPS technology for the consolidation of BG_Ca/Mix [14] and BGMS10 [18] allowed for the fabrication of nearly fully dense (relative density ≥ 99.7%) products, while completely avoiding devitrification phenomena during sintering. Table 1 also shows that similar findings were obtained with the (53.69 SiO_2, 33.23 CaO, 6.85 B_2O_3, 2.66 Al_2O_3, 2.63 Na_2O, 0.91 P_2O_5, mol.%) glass system, characterized by a crystallization temperature of about 850°C [20].

Among the recently developed bioactive glasses with reduced crystallization tendency, particular attention has been devoted to the Bio_MS composition (46.1 SiO_2, 31.3CaO, 5 Na_2O, 2.6 P_2O_5, 5 MgO, 10 SrO, mol %), obtained through the simultaneous incorporation of magnesium and strontium ions into a silicate glass network [26]. This formulation was specifically designed to combine improved thermal processability with the biological benefits associated with the controlled release of therapeutic ions. Magnesium plays a fundamental role in bone metabolism, promoting osteoblast proliferation and differentiation, extracellular matrix mineralization and regulation of apatite nucleation processes, while also contributing to the modification of the glass network structure and thermal behaviour [27,28]. Strontium is well known for its dual action on bone remodelling, being able to stimulate osteoblastic activity while reducing osteoclast-mediated bone resorption, thereby promoting bone formation and regeneration [29–31]. Consequently, the simultaneous release of Mg and Sr ions from bioactive glasses has been associated with enhanced osteogenic potential and improved biological performance compared with conventional formulations [7,8].

Table 1
State of the art for Bioactive Glasses (BGs) processed by Spark Plasma Sintering (SPS) with no additives: oxide composition, synthesis route, sintering conditions, crystalline phases, density, and mechanical properties (Hardness, Young's modulus).

BG type (oxides composition, mol.%)	T_C (°C)	Commercial or Lab-made BG (synthesis route)	SPS conditions (T_D/t_D/P)	Amorphous/ crystalline phases in bulk sample	Density, ρ	Mechanical properties Hardness (load), E	Reference
45S5 (46.1SiO_2, 26.9CaO, 24.4Na_2O, 2.6 P_2O_5)	~ 600	Commercial	850°C/ 10 min/ 40 MPa	n.r.	ρ= 100% (ρ_t=2.8 g/cm^3)	HV (n.r.) = 620 ± 11	[11]
		Lab-made (SG)	950°C/ 15 min/n.r.	Mainly crystalline ($Na_6Ca_3Si_6O_{18}$)	ρ= 92% (ρ_t=2.7 g/cm^3)	E = ~110 GPa	[12]
		Commercial	500–550°C/ 2 min/ 70–300 MPa	Mainly amorphous, $Na_2CaSi_2O_6$	ρ= 97.2–98.8% (ρ_t=2.7 g/cm^3)	n.r.	[13]
		Commercial	550°C/2 min/ 70 MPa	Mainly amorphous, $Na_6Ca_3Si_6O_{18}$	ρ= 100% (ρ_t=2.7 g/cm^3)	HV (1 N) = 905 ± 165 E = 82 ± 6 GPa	[14]
			600°C/2 min/ 16 MPa	Mainly crystalline ($Na_6Ca_3Si_6O_{18}$)	ρ= 99.3% (ρ_t=2.7 g/cm^3)	HV (1 N) = 810 ± 150 E = 67 ± 6 GPa	
		Commercial	500°C/3 min/ 50 MPa	Amorphous	ρ= 99.5% (ρ_t=2.72 g/cm^3)	Nanohardness= 6.45 ± 0.04 GPa E = 82.55 ± 0.03 GPa	[15]
			550°C/3 min/ 50 MPa	Mainly crystalline ($Na_2CaSi_3O_8$)	ρ= 100% (ρ_t=2.72 g/cm^3)	Nanohardness= 6.6 ± 0.1 GPa E = 96.3 ± 0.7 GPa	
			600°C/3 min/ 50 MPa	Mainly crystalline ($Na_2CaSi_3O_8$)	ρ= 100% (ρ_t=2.72 g/cm^3)	Nanohardness= 6.7 ± 0.2 GPa E = 98.1 ± 0.8 GPa	
		Commercial	1050°C/ 30 min/0 MPa	Mainly crystalline ($Na_6Ca_3Si_6O_{18}$, $NaCaPO_4$)	ρ= 97.6 ± 0.3% (ρ_t=2.7 g/cm^3)	HV (1.96 N) = 548.8 ± 38.5 HV (9.81 N) = 480.9 ± 25.7 E = 97.4 ± 3.6	[16]
		Commercial	550°C/3 min/ 50 MPa	Mainly crystalline ($Na_2CaSi_3O_8$)	n.r.	HV (4.9 N) = 810 ± 150 E = 90–100 GPa	[17]
BG_Ca/Mix (47.2SiO_2, 45.6CaO, 2.3Na_2O, 2.3 K_2O, 2.6 P_2O_5)	880	Lab-made (MQ)	730°C/2 min/ 70 MPa	Amorphous	ρ= 100% (ρ_t=2.76 g/cm^3)	HV (1 N) = 900 ± 180 E = 66 ± 4 GPa	[14]
			850°C/2 min/ 16 MPa	Mainly crystalline ($\alpha CaSiO_3$, $\beta CaSiO_3$)	ρ= 100% (ρ_t=2.76 g/cm^3)	HV (1 N) = 800 ± 150 E = 121 ± 6 GPa	
BGMS10 (47.2SiO_2, 25.6CaO, 10MgO, 10SrO, 2.3Na_2O, 2.3 K_2O, 2.6 P_2O_5)	932	Lab-made (MQ)	750°C/2 min/ 16 MPa	Amorphous (100 wt%)	ρ= 99.7% (ρ_t=2.97 g/cm^3)	HV (0.1 N) = 671.7 ± 16.6 E = 90.92 ± 3.42 GPa	[18]
			850°C/2 min/ 16 MPa	Amorphous (97.9 wt%), $\alpha CaSiO_3$ (1.1 wt%), $\beta CaSiO_3$ (1 wt%))	ρ= 99.3% (ρ_t=2.97 g/cm^3)	HV (0.1 N) = 718.8 ± 29.4 E = 92.80 ± 2.22 GPa	
			950°C/2 min/ 16 MPa	Amorphous (5 wt %), $\alpha CaSiO_3$ (71 wt%), $\beta CaSiO_3$ (21 wt%)	ρ= 98.6% (ρ_t=2.97 g/cm^3)	HV (0.1 N) = 619.2 ± 47.1 E = 98.38 ± 5.90 GPa	
BG-Bx (27.43–42.34SiO_2, 26.37–27.13CaO, 23.86–24.54Na_2O, 0.0–18.21B_2O_3, 2.61-2.68P_2O_5)	510	Lab-made (MQ)	420°C/2 min/ 50 MPa	Amorphous	ρ= 98.76–98.93% (ρ_t=2.7 g/cm^3)	E = 27.1–73.8 GPa	[19]
(52.21–53.69SiO_2, 6.85–7.83B_2O_3, 2.66–3.81Al_2O_3, 24.79–33.23CaO, 2.59–2.63Na_2O, 0.80-0.91P_2O_5, 0.0–0.21Fe_2O_3)	854–865	Lab-made (MQ)	520°C/0 min/ 28 MPa)	Amorphous	ρ= 99.27–100% (ρ_t=2.73–3.02 g/cm^3)	HV (0.49 N)= 630–770	[20]
58S-derived (60SiO_2, 28.5–36CaO, 0.0–2.5Ce_2O_3, 0.0–5.0CoO, 4 P_2O_5)	n.r.	Lab-made (SG)	650°C/5 min/ 50 MPa	Amorphous (>95%)	ρ= 98–99% (ρ_t=2.20–2.32 g/cm^3)	Nanohardness (4mN)= 2.5–5.6 GPa E = 43–75 GPa	[21]

E: Young's modulus, MQ: Melt-Quenching; SG: Sol-Gel derived; T_C = crystallization temperature; ρ_t=theoretical density; n.r.: not reported

Beyond its favourable therapeutic-ion release profile, Bio_MS exhibits an exceptionally attractive combination of thermal stability and biological responsiveness. It was demonstrated that this glass possesses a crystallization temperature of approximately 860 °C and a remarkably wide processing window, thus enabling thermal treatments while largely preserving the amorphous nature of the material. At the same time, Bio_MS showed rapid hydroxyapatite formation, excellent cytocompatibility and enhanced osteogenic differentiation of human bone marrow mesenchymal stromal cells, highlighting its strong regenerative potential [26]. Subsequent in vivo investigations confirmed its osteoconductive behaviour and biocompatibility, demonstrating effective bone regeneration and tissue integration in a rabbit femoral defect model [32]. More recently, Bio_MS was also shown to promote endothelial cell adhesion, proliferation and viability, while inducing a significant pro-angiogenic response both in vitro and in vivo, thereby highlighting its ability to support biological processes that are crucial for successful tissue regeneration [33].

The combination of high thermal stability, a wide processing window and outstanding biological performance makes Bio_MS a particularly attractive candidate for the fabrication of dense bioactive devices through advanced sintering technologies. Moreover, Bio_MS represents a composition already validated through extensive biological investigations, including osteogenic, osteoconductive and angiogenic studies, making it an ideal model system to evaluate whether advanced processing routes can preserve and possibly tailor its therapeutic functionality. Despite these promising features, no information is currently available on the response of Bio_MS to Spark Plasma Sintering, nor on the possible effects of SPS-induced densification and devitrification on its mechanical and biological performance.

Addressing these aspects is essential to understand whether the outstanding biological potential of Bio_MS can be successfully translated into mechanically reliable bulk devices suitable for bone tissue engineering applications.

Therefore, the aim of the present work is to investigate, for the first time, the Spark Plasma Sintering behaviour of Bio_MS glass powders over a wide temperature range. Particular attention is devoted to identifying the processing conditions capable of maximizing densification while controlling crystallization phenomena, as well as to correlating the resulting microstructural evolution with mechanical properties, ion-release kinetics and in vitro bioactivity. The results are finally discussed in comparison with those previously reported for 45S5, BG_Ca/Mix and BGMS10 glasses, providing further insight into the design of next-generation therapeutic-ion-releasing bioactive glasses specifically tailored for SPS-based manufacturing routes.

2. Experimental materials and methods

2.1. Processing

The bioactive Bio_MS glass (46.1 SiO_2, 31.3 CaO, 5 Na_2O, 2.6 P_2O_5, 5 MgO, 10 SrO, mol.%) was prepared by using the melt-quenching technique from commercial raw reagents (SiO_2, $Ca_3(PO_4)_2$, Na_2CO_3, $CaCO_3$, $SrCO_3$, and $MgCO_3$), following the procedure described elsewhere [26].

Sintering experiments were performed using a SPS apparatus (515S model, Fuji Electronic Industrial Co., Ltd., Kanagawa, Japan) operating under vacuum conditions (about 20 Pa) and temperature control. Proper amounts of Bio_MS (1.53 g) powders were loaded in a graphite die (Atal Srl., Italy; 15 mm inner diameter; 35 mm external diameter; 40 mm height). During SPS runs, temperature was measured with a K-type thermocouple (TC Misure e Controlli S.R.L., Italy) introduced into a small hole drilled on the external surface of the die. Samples were first heated at a rate of 50 °C/min until 100°C below the dwell temperature (T_D) was reached. Then, to prevent possible temperature overshooting, the heating rate was decreased to 10 °C/min. The duration of the isothermal stage at T_D was set to 2 min, after which the sample was cooled to 300°C at a rate of 50 °C/min, followed by natural cooling. The effect of the dwell temperature was investigated in the range 650–900°C while the applied pressure was maintained relatively low (P = 16 MPa), to avoid samples breakage.

Before being further characterized, sintered products were ground using progressively finer abrasive papers to remove residual graphite from their surface. Samples of about 14.7 mm diameter and 3 mm height were finally obtained. Each experimental condition was replicated at least twice. Additional info on the SPS procedure is reported in detail in previous works [25,34].

2.2. Characterization

The particle size distribution of the Bio_MS powders to be processed by SPS was determined by laser light scattering analysis (CILAS 1180, France).

Phase composition and microstructural features of powders and sintered samples were determined by X-ray Diffraction (XRD) using a Bruker D8 Advance diffractometer (Bruker, Germany) over a range of scattering angles 2θ from 20° to 120°, in steps of 0.05° with 15 s acquisition time per angle step. The Rietveld procedure was used to estimate phases content (wt%) and related microstructural parameters by analyzing XRD patterns with the MAUD program [35]. The amorphous phase fraction was calculated using a pseudo-crystalline structure factor ($Ca_{1.5}Na_{2.64}Si_9O_3$ phase; symmetry: trigonal; space group: R-3 m; crystallite size: 20 Å; microstrain: 0.03) according to the LeBail approach [36].

The thermal behavior of the glass powders was evaluated performing differential thermal analysis (DTA) experiments (Netzsch Differential Thermal Analyzer, DSC 404, Netzsch-Geräbau GmbH, Selb, Germany) from room temperature to 1000°C in air flow. DTA data recorded at different heating rates (8–30 °C/min) allowed us to estimate the effective activation energy of the crystallization process ($\boldsymbol{E_c}$) using the Kissinger's theory [37], according to the following expression:

$$\ln\left(\frac{r}{T_p^2}\right) = -\frac{E_c}{RT_p} + C \quad (1)$$

where $\boldsymbol{T_p}$(K) is the temperature value of the exothermic peak in the DTA curve, $\boldsymbol{r}$ is the heating rate, and $\boldsymbol{R}$ is the universal gas constant.

The absolute density of the sintered samples was measured according to Archimedes' principle employing an analytical balance (Ohaus Explorer Pro, Ohaus Corporation, NJ, USA) (± 0.0005 g precision) and ethanol as the liquid medium. To evaluate the relative density, the theoretical value of 3.01 g/cm^3 for Bio_MS was used, as previously determined by means of a gas pycnometer (Accupyc II 1340, Micromeritics, USA) [10].

2.3. Mechanical properties

The mechanical properties of the sintered Bio_MS samples were determined using an Open Platform micro-indentation system (CSM Instruments, Peseux, Switzerland), equipped with a Vickers diamond tip. Vickers hardness (HV) and Young's modulus (E_{IT}) were measured by performing indentations up to a maximum applied load of 0.25 N, employing loading and unloading rates of 0.5 N/min and maintaining the peak load for 15 s. At least fifteen indentations were performed, while the corresponding load–displacement curves were continuously acquired during each test. The E_{IT} values were subsequently derived according to the Oliver–Pharr approach [38].

2.4. In-vitro tests

The *in vitro* bioactivity of the sintered Bio_MS was assessed through a semi-dynamic immersion test in Simulated Body Fluid (SBF), according to the method proposed by Kokubo et al. [39]. Specifically, the Bio_MS disks (respectively sintered at 900 °C, 815 °C, and 750 °C) were

immersed in SBF and maintained at 37 °C for predetermined periods of 1, 3, and 7 days. Each disk was immersed in 20 mL of SBF, corresponding to an exposed-surface-area-to-solution-volume ratio of approximately 15 mm^2/mL. After each soaking period, the samples were recovered, rinsed with distilled water, and left to dry at room temperature for approximately 24 h. During the test, the pH of the solution, initially adjusted to 7.4 in accordance with the standard Kokubo procedure, was periodically monitored at 37 °C. In addition, the SBF solution was completely refreshed every 48 h to maintain stable testing conditions. The morphology and elemental composition of the immersed samples were subsequently characterized by field-emission scanning electron microscopy (FEG-SEM; Nova NanoSEM 450, FEI-ThermoFisher Scientific, Eindhoven, The Netherlands) coupled with energy-dispersive X-ray spectroscopy (EDS; Quantax-200, Bruker Nano GmbH, Berlin, Germany). Moreover, the soaked samples were analysed by Raman spectroscopy to identify the formation of hydroxyapatite (HAp)-like calcium phosphate precipitates.

2.5. Ion release measurements

The release of ionic species from the sintered samples was investigated through an *in vitro* dissolution study performed in SBF. For each immersion period (1, 3, and 7 days), all samples were incubated at 37 °C under static conditions. At the end of each soaking period, the collected solutions were analysed by Inductively Coupled Plasma Triple Quadrupole Mass Spectrometry (iCAP TQ ICP-MS, Thermo Fisher Scientific, Bremen, Germany). To improve analytical accuracy and minimize non-spectral interferences, scandium was employed as an internal standard. Quantification was performed using calibration curves prepared from certified ionic standards, and all samples were analysed after appropriate dilution.

3. Results and discussion

3.1. Powders characterization

The particle size parameters of the Bio_MS powders used in this work for SPS processing are d_{10}= 0.85 ± 0.01, d_{50}= 4.60 ± 0.13, d_{90}= 24.47 ± 0.57, and $d_{(4,3)}$ = 9.01 ± 0.23 μm. These data are consistent with SEM observation, whose images are shown in Fig. 1. Irregularly shaped particles with sizes ranging from less than 1 μm to above 10 μm can be seen.

The thermal behaviour of these powders was investigated at different heating rates, in the range 8–30 °C/min, by DTA. From the resulting curves plotted in Fig. 2**(a)**, it is seen that the characteristic crystallization peak shifts towards higher temperatures with increasing heating rate, i.e. from about 883°C (8 °C/min) to 922 °C (30 °C/min).

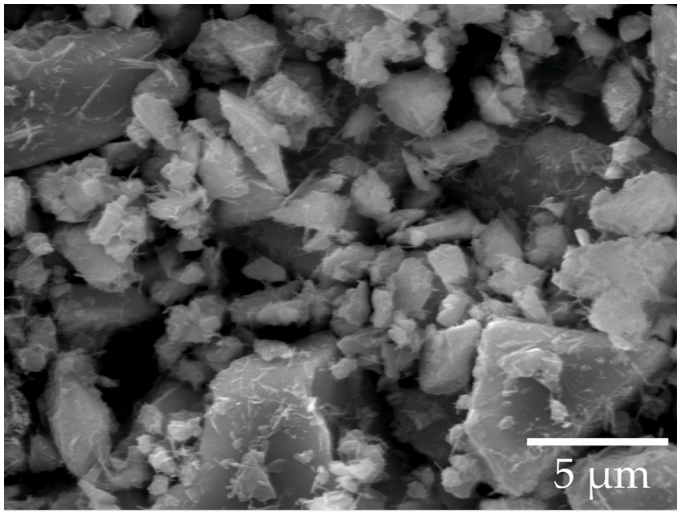


Fig. 1. SEM image of Bio_MS powders used in this work for the preparation of bulk samples.

When plotting these data in the form of $\left(\frac{r}{T_p^2}\right)$ as a function of $\left(\frac{1}{T_p}\right)$ (cf. Eq. 1), the straight line shown in Fig. 2**(b)** is obtained. From the corresponding slope, the effective activation energy E_c of about 370 kJ/mol associated with the crystallization of Bio_MS glass was then estimated. Such value is higher with respect to the reported literature data for standard Bioglass® and S53P4 glasses, in the range of 230–338 and 283–311 kJ/mol, respectively [37].

In this regard, it should be noted that, in principle, the Matusita–Sakka approach [40] is more rigorous than the Kissinger method since the former accounts for the specific mechanisms of crystal nucleation and growth by including two parameters, the Avrami exponent (n) and the dimensionality of growth (m), as follows:

$$\ln\left(\frac{r^n}{T_p^2}\right) = -\frac{mE_c}{RT_p} + C \tag{2}$$

However, the critical particle size for the transition from surface to bulk crystallization mechanisms typically occurs in the range 100–150 μm. Since the average size ($d_{(4,3)}$ = 9.01 ± 0.23 μm), and even the coarsest fraction (d_{90}=24.47 ± 0.57μm), of the Bio_MS glass powders studied in this work are well below that limit, it can be stated that the entire powder strictly falls within the surface crystallization regime, for which $m = n = 1$ can be assumed [40]. Consequently, within the scenario examined in the present study, the Eq. (2) converges to that of Kissinger, Eq. (1).

The estimated E_c value further supports the lower crystallization tendency of the Bio_MS composition with respect to conventional glass formulations. This holds also when considering other recently developed glasses in the (SiO_2–B_2O_3–Al_2O_3–CaO–Na_2O–P_2O_5) system, which show activation energy values in the range 292–324 kJ/mol [20].

In particular, the high crystallization stability of Bio_MS can be related to its specific network-forming and network-modifying composition. The relatively high SiO_2 content (46.1 mol%) contributes to the formation of a strongly interconnected silicate network, while the relatively low Na_2O content (5 mol%) limits the depolymerization of the network typically promoted by alkali modifiers [41,42]. Consequently, a comparatively polymerized and structurally stable glass network is expected, making the structural rearrangements required for nucleation and crystal growth more difficult.

Furthermore, the presence of MgO (5 mol%) and SrO (10 mol%) is expected to contribute to the stabilization of the glass network [27,43–45]. Compared with highly mobile alkali modifiers, these divalent cations interact more strongly with the silicate network and can increase the structural constraints associated with atomic rearrangement during crystallization [46]. Therefore, a higher thermal energy is required to promote the structural rearrangements necessary for the formation and growth of crystalline phases [46]. This provides a possible explanation for both the high crystallization temperature and the relatively high activation energy determined for Bio_MS.

The same compositional–structural interpretation can be considered when comparing Bio_MS with other glasses reported in the literature [37]. Materials characterized by higher concentrations of alkali modifiers and/or a less polymerized network are generally expected to exhibit greater structural mobility and, consequently, lower energetic barriers for crystallization. Conversely, the combination of a relatively high network-former content, limited alkali modification, and the presence of divalent modifiers in Bio_MS results in a more thermally stable glass network, which can account for its higher resistance to crystallization [43,47].

On the other hand, the relatively lower E_c value of Bio_MS compared to that estimated for the previously investigated BGMS10 formulation

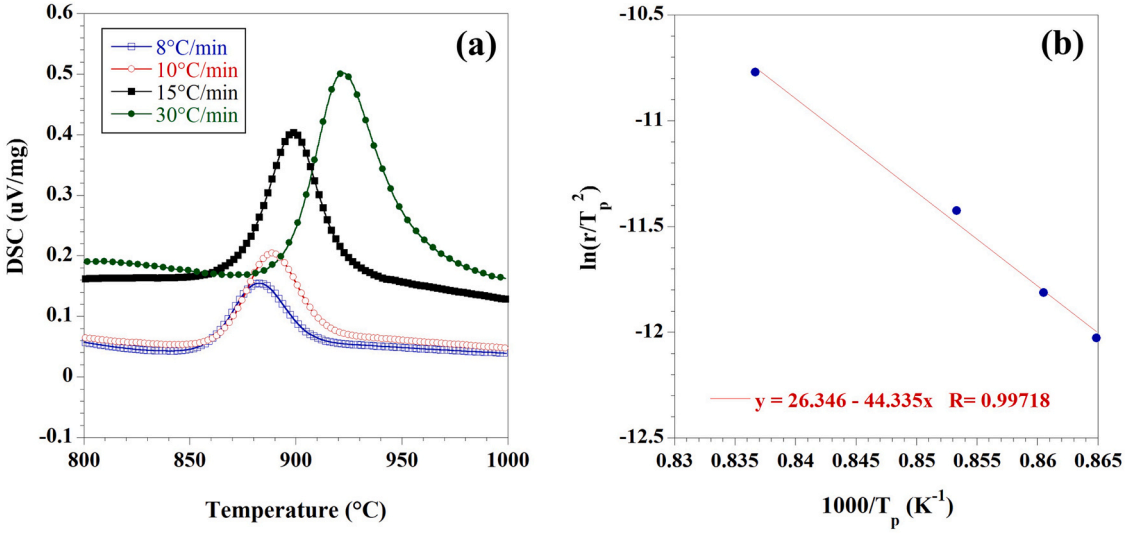


Fig. 2. DTA curves (a) of Bio_MS powders at different heating rates and (b) corresponding Kissinger plot.

(538.9 kJ/mol) [18] is consistent with their corresponding crystallization temperatures, i.e. 859 °C [26], and 932 °C [25], respectively.

3.2. Sintered samples

The effect of the sintering temperature on the densification and compositional/microstructural changes of Bio_MS samples was first investigated. According to previous studies on similar glass systems [18], the holding time and the applied pressure were maintained equal to 2 min and 16 MPa, respectively. In particular, the use of higher mechanical pressure was avoided to prevent samples breakage during SPS. Fig. 3 (red line) shows that the bulk density progressively increased from about 2.82–2.99 g/cm^3 (equivalent to an increase in relative density from 93.6% to 99.3%) as T_D was raised from 650 to 800°C. A further increase of the sintering temperature up to 900°C led to nearly fully dense samples (99.65%).

Compositional and microstructural changes occurring when Bio_MS powders were processed at different temperatures by SPS were investigated by XRD analysis (Fig. 4). The diffraction patterns of samples produced up to T_D= 800°C are characterized by the halo peak typical of an amorphous glass, as observed for the starting powders. As reported in our past works [18,34], also in the present study the glass phase was

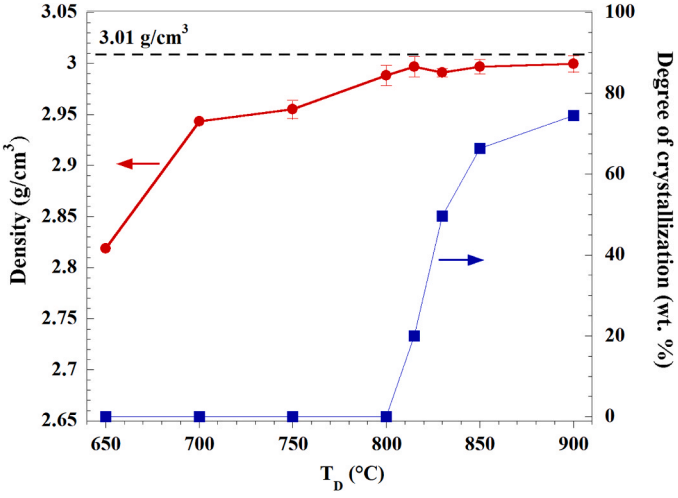


Fig. 3. Influence of the dwell temperature on the density and degree of crystallization of Bio_MS samples produced by SPS (t_D=2 min, P = 16 MPa).

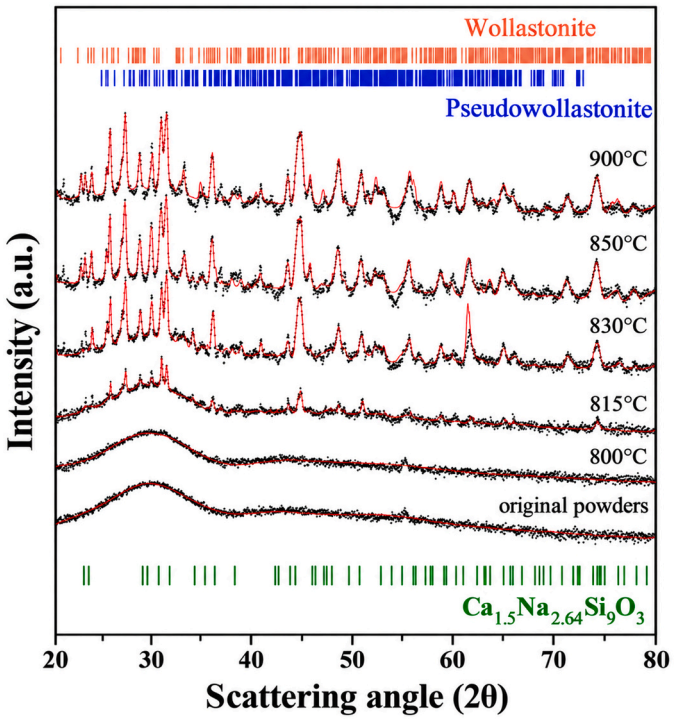


Fig. 4. XRD patterns of Bio_MS samples sintered at various temperatures. Original glass powders data are also shown for the sake of comparison. Black dots are experimental data; the red line is the calculated fit. The bar sequence marks the expected peak positions from the values of lattice parameters and space group of the crystallographic phases. Details on the amount of each phase and related microstructural parameters are reported in supplementary Table S1.

described as $Ca_{1.5}Na_{2.64}Si_9O_3$, which was modelled using a pseudo-crystalline structure factor ($Ca_{1.5}Na_{2.64}Si_9O_3$ phase; symmetry: trigonal; space group: R-3m; crystallite size: 20 Å; microstrain: 0.03) following the LeBail approach [36].

The XRD pattern of the sample sintered at 815 °C is still dominated by the amorphous peak but some Bragg reflections start to appear (Fig. 4). Based on Rietveld analysis, whose results are reported in supplementary Table S1, these peaks are associated with two polymorphs of $CaSiO_3$ (β-$CaSiO_3$, wollastonite, triclinic *P-1*, α-$CaSiO_3$ and

pseudowollastonite, monoclinic *C2/c*), whose amounts were estimated to be about 15.2 and 4.8 wt%, respectively. Crystallization phenomena proceeded as the sintering temperature was progressively increased. Thus, the amorphous fraction present in SPS samples obtained at 830°C was reduced to 50.4 wt%, to form mostly pseudowollastonite (29.9 wt %) and, albeit in smaller amounts, wollastonite (19.7 wt%). This trend continued as the temperature was further increased. Finally, pseudowollastonite was the dominant phase (61.4 wt%) found in the Bio_MS derived sample produced at 900°C, followed by the amorphous one (25.5 wt%), and wollastonite (13.1 wt%) (supplementary Table S1).

The crystallization degree in SPS specimens is plotted in Fig. 3 as a function of the dwell temperature (blue line). Highly dense (>99%) and fully amorphous Bio_MS samples can be obtained by SPS at 800°C, while equally dense but partially crystallized samples resulted when operating at higher temperatures.

The structural/compositional changes of the glass powders undergoing SPS as discussed above are also responsible for the change in colour of the resulting bulk samples (Fig. 5). The 93.3% dense sample sintered at 650°C showed only slight darkening compared with the initial white Bio_MS powders. In contrast, as the T_D value was raised from 700 to 800 °C, the resulting highly dense, and still amorphous, products display a progressive and marked darkening. However, at sintering temperatures at or above 815°C, the samples behave in the opposite way and become progressively lighter in colour. This agrees with similar findings from our previous studies on other glass systems [18] and can be explained as follows. The whitish visual appearance of the sample sintered at 650°C can be readily attributed to its residual porosity, which induces light scattering. As the sintering temperature increases progressively without inducing devitrification (700–800°C range), the pores are gradually eliminated (with the relative density increasing from 97.77% to 99.51%), thereby reducing the latter effect. As observed in Fig. 4, the onset of crystallization occurs at 815°C; the nucleation of the newly formed crystals causes a refractive index mismatch between the crystals and the glass matrix. Consequently, light scattering is re-induced, making the sample appear slightly lighter than the non-crystallized one produced at 800°C. This phenomenon becomes progressively more pronounced as the temperature is raised from 830°C to 900°C, a range in which the degree of crystallization in the sintered sample gradually increases up to 74.5 wt%. It is worth noting that within the 800–900°C temperature range, the densification level of the SPS samples varies only minimally (between 99.51% and 99.65%). Therefore, porosity plays no role in light scattering within this interval.

3.2.1. Mechanical properties

The results of the microindentation tests performed under a maximum load of 250 mN are summarized in Table 2. Both HV and E_{IT} values agree with those previously reported in the literature for BGs with comparable compositions [18,34,48]. However, the mechanical properties were found to vary depending on the sintering conditions. In particular, the specimen treated at 900 °C exhibited higher HV and E_{IT} values compared with the samples sintered at lower temperatures. For hardness (HV), the ranking was 900 °C > 750 °C > 815 °C, whereas for indentation modulus (EIT) it was 900 °C > 815 °C > 750 °C.

In contrast to the elastic modulus, which progressively increases with increasing sintering temperature, Vickers hardness is strongly affected by local plastic deformation, residual porosity, microstructural heterogeneity, phase evolution, and residual stresses [49]. Therefore, the lower Vickers hardness measured for the Bio_MS sample sintered at 815 °C can be attributed to the microstructural evolution occurring in this intermediate sintering-temperature range.

Table 2
Vickers hardness (HV) and Young's Modulus (E_{IT}) measured at a maximum indentation load of 0.25 N of the SPS sintered Bio_MS samples at three different temperatures: 900 °C, 815 °C, and 750 °C.

Sample	Vickers Hardness (HV)	Elastic Modulus E_{IT} (GPa)
Bio_MS 900 °C	828.8 ± 53.4	108.3 ± 3.9
Bio_MS 815 °C	686.4 ± 64.6	100.3 ± 4.7
Bio_MS 750 °C	758.3 ± 38.2	93.16 ± 2.9

At 750 °C, the relatively low hardness may be mainly associated with incomplete densification and the presence of residual porosity. Upon increasing the SPS temperature to 815 °C, the Bio_MS structure promotes structural rearrangement and the onset/partial development of crystalline domains within the glassy matrix. Such a partially crystallized and heterogeneous microstructure may introduce glass/crystal interfaces and residual stresses, which can locally facilitate deformation and crack initiation during indentation. Consequently, the sample processed at 815 °C exhibits the lowest Vickers hardness, despite its higher elastic modulus compared with the sample sintered at 750 °C. On the other hand, at 900 °C, the more advanced structural evolution and increased densification lead to a more consolidated microstructure and a reduced contribution of residual porosity.

Crystallization is considered to have a disadvantageous effect on bioactive glasses on several levels, and, in many cases, the crystallization of bioactive glasses takes place before significant densification can be achieved through sintering [50]. Therefore, the non-linear trend in Vickers hardness may be attributed to the competition between densification and crystallization phenomena occurring during SPS.

Moreover, the findings reveal that the mechanical properties of the Bio_MS were slightly higher than those reported in similar studies [51, 52]. This can be attributed to the addition of Mg and Sr ions. In fact, these ions can affect the network structure, improving the mechanical properties of the BGs [51].

3.2.2. Bioactivity behaviour

The *in vitro* bioactivity of the sintered Bio_MS samples was evaluated through SBF immersion tests by monitoring the pH evolution and analysing the surface modifications occurring during soaking. The pH behaviour is characteristic of BGs and is related to the ionic exchange between alkali and alkaline-earth ions released from the glass network, mainly Na^+ and Ca^{2+}, and H_3O^+ ions from the surrounding solution [53, 54]. This process promotes the dissolution of the glass surface, the formation of silanol groups (Si–OH), and the consequent alkalization of the medium [39,53,54]. At longer immersion times, the pH values tended to stabilize, indicating the gradual establishment of equilibrium between dissolution and precipitation phenomena [53].

For all the investigated samples, the pH of the solutions progressively increased with immersion times, with the largest increase occurring between 48 and 96 h (Fig. 6). The extent of the pH variation was strongly affected by the sintering temperature. In particular, the sample sintered at 750 °C showed the highest increase in pH, suggesting a greater initial dissolution rate and higher surface reactivity. The sample sintered at 815 °C displayed an intermediate behaviour, although very similar to that of the sample sintered at 750 °C. Conversely, the sample

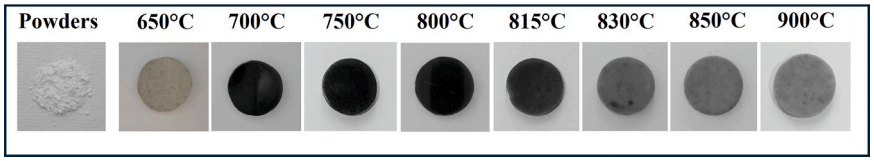


Fig. 5. Optical images of initial Bio_MS powders and the corresponding bulk samples produced by SPS at different T_D values (P = 16 MPa, t_D=2 min).

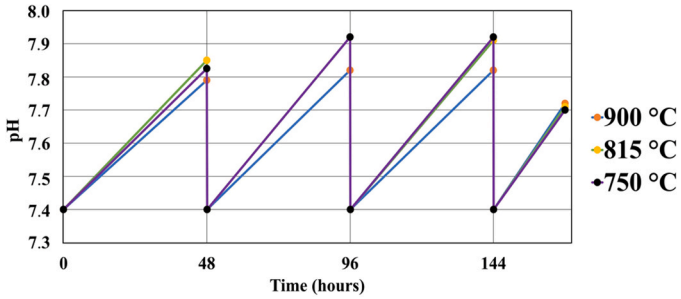


Fig. 6. pH variation induced by the sintered samples at 750 °C (violet), 815 °C (green), and 900 °C (blue).

sintered at 900 °C exhibited a less pronounced pH increase, which can be associated with the combined effect of increased densification and partial crystallization induced by the thermal treatment, resulting in a lower reactive surface area and reduced ion release.

The *in vitro* bioactivity of a BG, in particular its ability to induce HAp formation, can be assessed using Raman spectroscopy. The results of the analysis are reported in Figs. 7–9, which illustrate the Raman spectra of Bio_MS samples before immersion and after 1, 3, and 7 days of soaking in SBF. The Raman spectra were analyzed in the 200–1200 cm^{-1} region, as this interval encompasses the main vibrational bands of both silicate glasses and HAp. The spectra confirmed the progressive formation of calcium phosphate phases, which evolve into an HAp-like phase on the sample surfaces during immersion in SBF.

In particular, the non-immersed Bio_MS sample, heat-treated at 750 °C and therefore remaining largely amorphous (Fig. 7), exhibited the broad Raman features typically observed in Na_2O–CaO–SiO_2-based glasses [55]. A broad band centered at approximately 620–635 cm^{-1} can be attributed to vibrations of the silicate network, with its exact position depending on the SiO_2 content of the glass [56]. The spectrum is dominated by an intense band at around 950–960 cm^{-1}, commonly attributed to the symmetric stretching vibration of PO_4 groups, although overlapping contributions from depolymerized silicate species cannot be excluded. This intense feature partially obscures weaker silicate-related contributions in the 800–1150 cm^{-1} region, which are observed only as broad shoulders, particularly on the high-wavenumber side of the main peak. The predominance of broad Raman features and the absence of sharp peaks are consistent with the predominantly amorphous character of the sample.

The Raman spectra of the non-immersed Bio_MS samples reveal a progressive devitrification of the glass with increasing heat-treatment temperature. While the sample treated at 750 °C displays broad bands characteristic of an amorphous glassy network, the spectrum recorded after treatment at 815 °C (Fig. 8) shows the onset of structural ordering, as evidenced by the narrowing and improved resolution of some Raman features. Extensive crystallization is observed at 900 °C (Fig. 9), where numerous sharp and well-defined peaks indicate the transformation of the parent glass into a glass-ceramic material. The marked increase in spectral resolution and the appearance of well-defined vibrational modes are consistent with the extensive crystallization revealed by the XRD-Rietveld analysis (see Fig. 4), which identified pseudowollastonite as the predominant phase, together with smaller amounts of wollastonite and a residual amorphous fraction.

The first Raman signals attributable to HAp-like phase formation were already faintly detectable after 1 day of immersion. The intensity of these bands progressively increased after 3 days and, even more markedly, after 7 days, demonstrating the continuous growth of an apatite layer on the sample surface.

For the Bio_MS sample sintered at 750 °C after 7 days of immersion (Fig. 7), the Raman spectrum exhibits the characteristic features of an HAp-like phase precipitated in vitro. In particular, the bands associated with Si–O–Si stretching vibrations become less intense, while the band related to PO_4 groups shifts towards higher wavenumbers, reaching approximately 960 cm^{-1}, and shows a marked increase in relative intensity. This band, which can be considered a distinctive spectroscopic signature of apatite phases, is assigned to the totally symmetric stretching mode of PO_4 tetrahedra. Additional bands emerge at approximately 590 cm^{-1} and 430 cm^{-1}, corresponding to the bending modes of the PO_4 group, while a further peak appears at about 1070 cm^{-1}. This latter feature is attributed to carbonate groups and is not present in stoichiometric HAp, indicating that the apatite formed during in vitro testing is carbonated, as widely reported in the literature for bioactive materials exposed to physiological-like environments [57–59].

The kinetics of apatite formation were strongly influenced by the heat-treatment temperature and, consequently, by the degree of crystallization of the material. The sample sintered at 750 °C (Fig. 7), which retained a predominantly amorphous structure, exhibited the most rapid development of HAp-related Raman features. In particular, the intense band at ~960 cm^{-1} became the dominant spectral feature after 7 days of immersion, largely obscuring the contributions from the underlying glassy matrix. This behavior is consistent with the higher dissolution

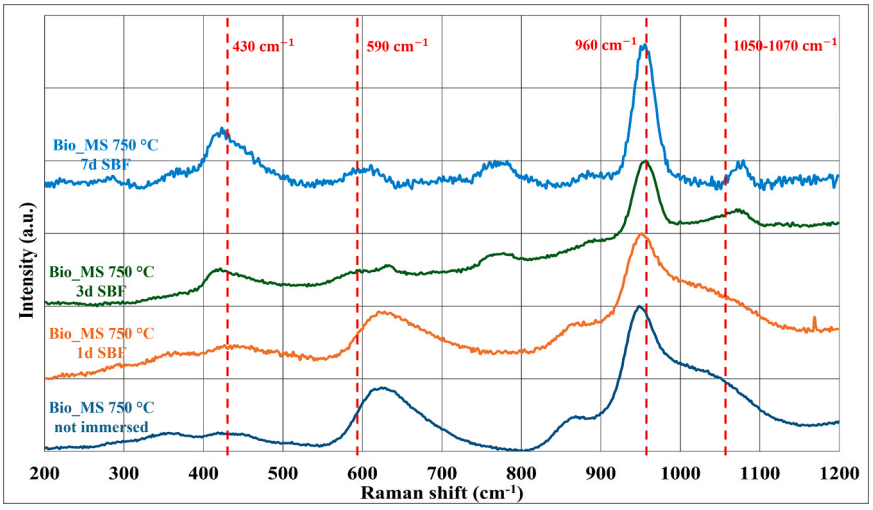


Fig. 7. Raman spectra of Bio_MS samples sintered at 750 °C before SBF immersion and after 1, 3, and 7 days of soaking in SBF. From bottom to top: sample before immersion (blue), and samples immersed for 1, 3, and 7 days (orange, green, and light blue, respectively). The red dashed lines indicate the characteristic Raman bands associated with HAp-like phase formation.

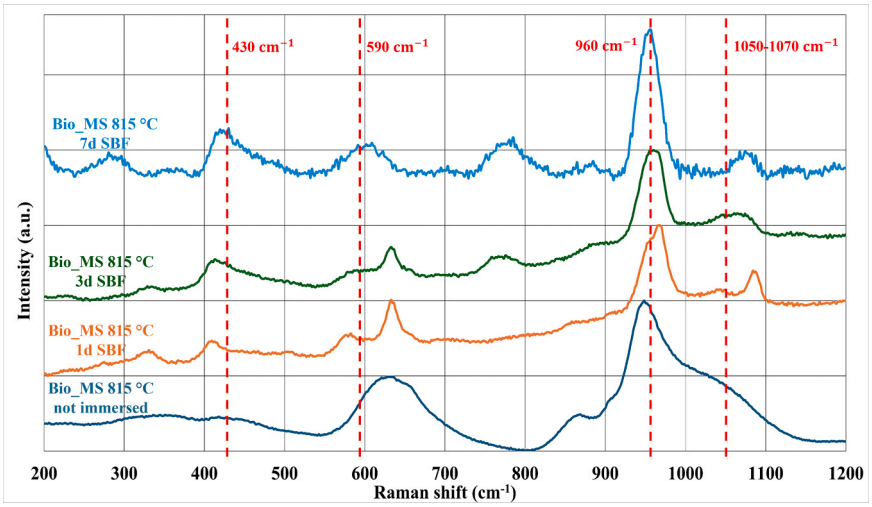


Fig. 8. Raman spectra of Bio_MS samples sintered at 815 °C before SBF immersion and after 1, 3, and 7 days of soaking in SBF. From bottom to top: sample before immersion (blue), and samples immersed for 1, 3, and 7 days (orange, green, and light blue, respectively). The red dashed lines indicate the characteristic Raman bands associated with HAp-like phase formation.

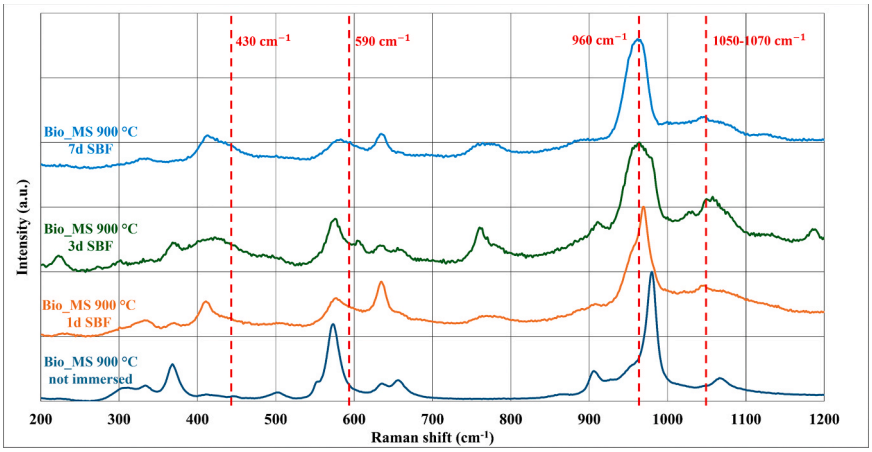


Fig. 9. Raman spectra of Bio_MS samples sintered at 900 °C before SBF immersion and after 1, 3, and 7 days of soaking in SBF. From bottom to top: sample before immersion (blue), and samples immersed for 1, 3, and 7 days (orange, green, and light blue, respectively). The red dashed lines indicate the characteristic Raman bands associated with HAp-like phase formation.

rate typically associated with amorphous bioactive glasses, which promotes a faster supersaturation of the surrounding medium with Ca^{2+} and PO_4^{3-} ions and, consequently, a more rapid precipitation of apatite.

In contrast, the samples treated at higher temperatures showed a slower evolution of the HAp-related bands. Although clear evidence of apatite formation was observed after 7 days of immersion, Raman features associated with the original crystalline phases remained detectable, particularly in the sample sintered at 900 °C (Fig. 9). This observation suggests that the higher degree of crystallization reduced the initial reactivity of the material and slowed the surface conversion process, while preserving its ability to develop a bioactive apatite layer over longer immersion times.

It is worth noting that the assignment of the reaction products as an HAp-like phase was based on the simultaneous observation of the characteristic phosphate vibrational modes at approximately 430, 590, and 960 cm^{-1} and of the carbonate-related band at approximately 1070 cm^{-1}, rather than on the 960 cm^{-1} band alone. The identification was further supported by the Ca- and P-rich deposits detected by SEM/EDS.

The surface morphology of the Bio_MS samples after 7 days of immersion in SBF was investigated by FEG-SEM and EDS analysis (Fig. 10). Additional images for immersion times of 1 and 3 days are reported in the Supplementary Materials (Fig. S1). In all cases, the presence of Ca- and P-containing deposits could be observed on the sample surfaces, indicating the occurrence of mineralization phenomena during soaking. The sample sintered at 750 °C (Fig. 10**a,b**) exhibits numerous globular precipitates distributed over the surface. In addition, the characteristic cracked and flake-like morphology observed over large areas of the sample is commonly reported for bioactive glasses after immersion in SBF and is generally associated with the formation of a hydrated silica gel layer. During the bioactivity process, dissolution of the glass network leads to the formation of a silica-rich hydrated layer, which acts as a favorable substrate for the subsequent nucleation and growth of calcium phosphate phases. Upon drying, this gel layer typically undergoes shrinkage, resulting in the formation of cracks and exfoliated regions. EDS analysis performed on the selected area confirms the presence of calcium and phosphorus, suggesting the formation of calcium phosphate reaction products. For the sample sintered at 815 °C (Fig. 10**c,d**), a similar morphology can be observed, with an extended cracked surface layer covered by fine granular deposits. The corresponding EDS spectrum reveals a marked presence of Ca and P, further supporting the precipitation of calcium phosphate phases. The Au peaks detected in the

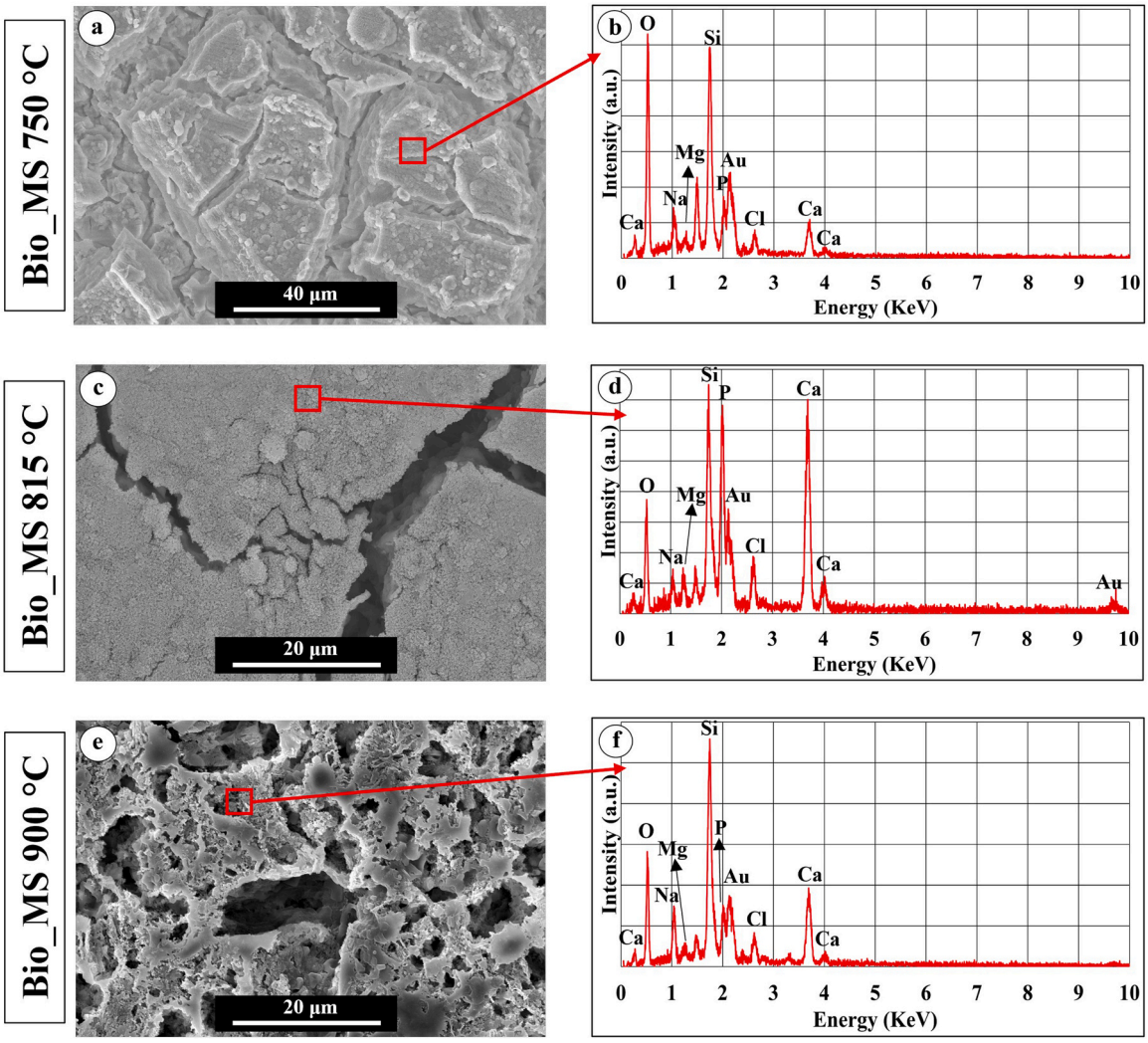


Fig. 10. FEG-SEM micrographs and EDS analyses of sintered Bio_MS samples after 7 days of soaking in SBF. The EDS spectra refer to the highlighted (red) areas shown in the micrographs. (a, b) 750 °C; (c, d) 815 °C; and (e, f) 900 °C.

spectrum originate from the conductive coating applied prior to SEM observation. The specimen sintered at 900 °C (Fig. 10**e,f**) shows a markedly different surface morphology, characterized by a porous reaction layer in which the typical cracked silica-gel appearance is less evident. EDS analysis again confirms the coexistence of calcium and phosphorus within the deposited phase, indicating that mineralization also occurred on the most crystallized material. The less pronounced development of the characteristic silica-gel morphology may suggest slower surface reaction kinetics, likely associated with the higher degree of crystallization of the sample.

Overall, SEM and EDS observations demonstrate that all SPS-processed Bio_MS samples retain the ability to promote the formation of Ca–P-rich deposits after immersion in SBF. These findings are consistent with the Raman spectroscopy results discussed in the previous section, which confirmed the formation of HAp-like compounds on the sample surfaces and suggested that the surface reaction kinetics were influenced by the sintering temperature.

It is worth noting that the samples analyzed in this study formed an apatite layer within 7 days in SBF, which is comparable to or faster than the 7–14 days reported for HAp formation in Sr/Mg doped or co-doped bioactive glass nanoparticles and markedly faster than the delayed apatite formation reported for Mg-containing glasses [29,60]. The retained bioactivity despite the presence of Mg confirms that MgO content in Bio_MS lies below the threshold at which Mg inhibits apatite nucleation and crystallization, consistent with the optimal balance reported by Moghanian et al. at ~5 mol% MgO [8,61].

3.2.3. *Ion release measurement*

The ICP-MS analysis of the investigated ionic species (Fig. 11) provided useful information on the dissolution behaviour of the BG samples and on their interaction with the physiological medium during immersion in SBF for 1, 3, and 7 days [62,63]. The obtained ion release trends were consistent with the pH, Raman, and SEM/EDS results discussed above and provided further information on the dissolution behaviour of the SPS-processed Bio_MS samples. Overall, the results confirmed the progressive dissolution of the glass network together with the simultaneous formation of calcium phosphate phases on the material surface.

Silicon release (Fig. 11**a**) progressively increased with immersion time for all samples, reflecting the gradual dissolution of the silicate network. However, the extent of Si release strongly depended on the sintering temperature. The sample sintered at 750 °C exhibited the highest silicon concentration at all investigated time points, followed by the specimen treated at 815 °C, whereas the lowest values were measured for the sample sintered at 900 °C. This trend is consistent with the different degrees of crystallization induced by SPS. The predominantly amorphous material obtained at 750 °C is expected to dissolve more readily, whereas the increasing crystallized fraction at higher temperatures reduces the dissolution rate.

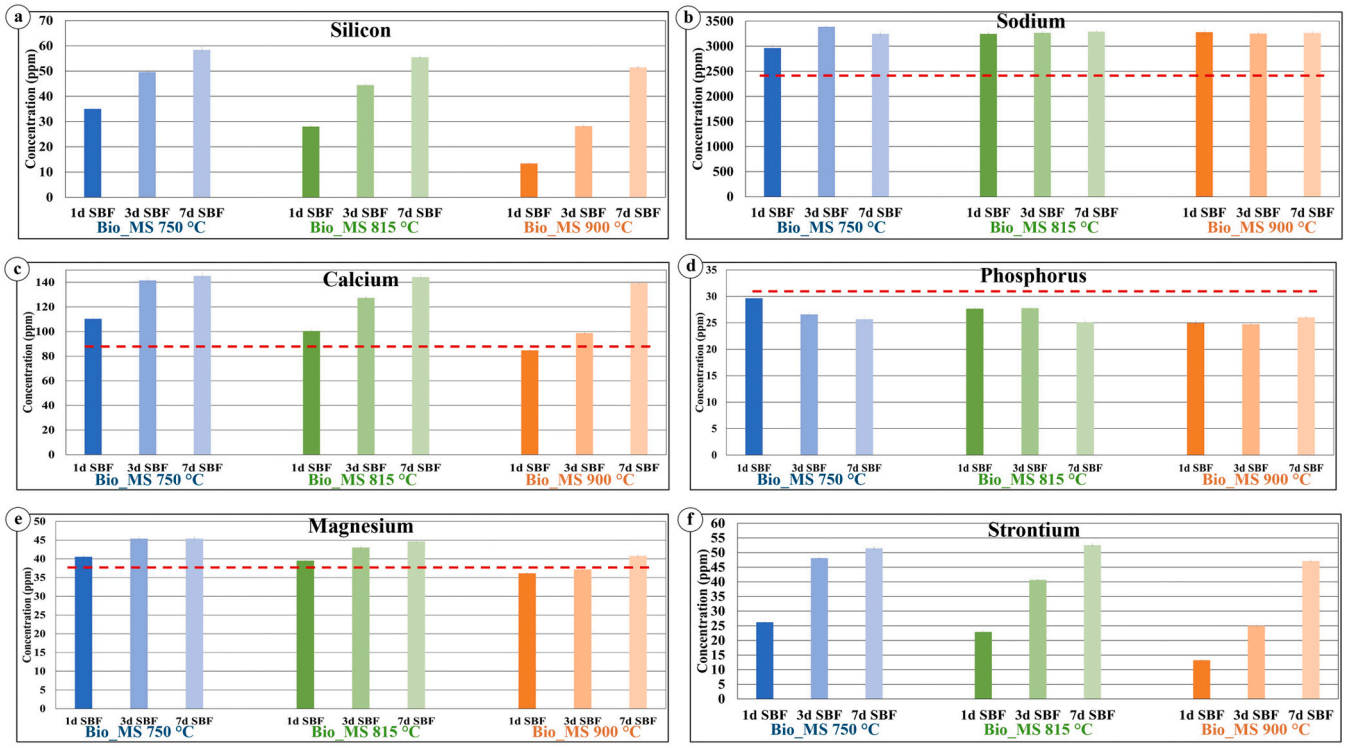


Fig. 11. Ion release measurements of sintered Bio_MS samples soaked 1, 3, and 7 days in SBF: (a) Silicon; (b) Sodium; (c) Calcium; (d) Phosphorus; (e) Magnesium; and (f) Strontium.

Sodium release (Fig. 11**b**) showed only limited variations among the investigated samples. This behavior is consistent with the relatively low Na_2O content of Bio_MS compared with conventional bioactive glasses such as 45S5 and reflects the rapid establishment of ion-exchange equilibria during the early stages of immersion.

Calcium release (Fig. 11**c**) followed the same general trend observed for silicon. The concentration of Ca in solution progressively increased with immersion time and was systematically higher for the samples sintered at lower temperatures. Calcium plays a key role in the bioactivity mechanism of silicate glasses, contributing to the supersaturation of the surrounding medium and promoting the precipitation of calcium phosphate phases. The greater calcium release observed for the 750 °C and 815 °C samples is therefore consistent with their higher reactivity.

Phosphorus exhibited the opposite trend (Fig. 11**d**). In all cases, its concentration remained below the initial value present in SBF and generally decreased with immersion time, indicating its progressive consumption during the formation of calcium phosphate deposits. This behavior agrees well with the Raman and SEM/EDS observations, which demonstrated the development of HAp-like phases on the sample surfaces. Interestingly, the sample sintered at 900 °C showed the most pronounced reduction in phosphorus concentration already after 1 day of immersion, while the calcium concentration remained close to the initial value present in SBF. This observation suggests that, at this early stage, the decrease in P should not be directly interpreted as evidence of HAp formation. Rather, it may reflect initial phosphate adsorption phenomena or the formation of early calcium-phosphate nuclei that have not yet evolved into a mature apatite layer. This interpretation is consistent with the slower surface reaction behavior observed for the most crystallized sample.

The release of magnesium and strontium (Fig. 11**e,f**) is particularly relevant because these ions are known to positively influence osteoblastic activity and bone regeneration processes [27,28]. Both ions showed a progressive increase in concentration with immersion time, confirming their continuous release from the glass matrix. In general, the release behavior followed the same trend observed for silicon and calcium, with lower sintering temperatures promoting greater ion dissolution. However, unlike Si and Ca, the differences among the samples were less pronounced for Mg and, especially, for Sr. Interestingly, the specimen sintered at 815 °C exhibited Sr concentrations comparable to, or even slightly higher than, those measured for the fully amorphous sample after longer immersion times. This observation suggests that crystallization does not simply reduce the overall ion release but may also modify the release kinetics of specific cations through changes in phase composition and microstructure. Therefore, partial devitrification appears capable of modulating the delivery of therapeutic ions while maintaining significant Sr and Mg release.

In general, ion release values are consistent with the diffusion-controlled kinetics reported by Fredholm et al. for Sr-substituted glasses, where Sr release increases linearly with Sr content and Si/Sr concentrations scale with the square root of time in the early stages [62]. Notably, whereas Mg is known to retard dissolution when present at high concentrations, our 5 mol% MgO content preserves a relatively high ion release, in line with the low-substitution regime identified by Wetzel et al. for 45S5 [64].

Overall, the ICP-MS results demonstrate that the degree of crystallization induced by SPS directly influences the dissolution behavior of Bio_MS. Lower sintering temperatures favor ion release and accelerate the development of a bioactive surface, whereas higher temperatures lead to a more controlled dissolution process while still preserving the ability of the material to release therapeutic Mg and Sr ions and promote HAp-like phase formation. These findings further support the possibility of tailoring the biological response of Bio_MS through SPS-induced microstructural modifications, balancing bioactivity, ion release, and mechanical performance.

4. Concluding remarks

The successful consolidation of the Mg and Sr co-doped Bio_MS glass via Spark Plasma Sintering demonstrates that the historical trade-off between achieving high material density and maintaining an

amorphous, highly bioactive state can be effectively overcome. Taking advantage of an exceptionally wide sintering window and a high activation energy for crystallization (370 kJ/mol), this BG composition allows for the fabrication of nearly fully dense bulk structures while completely preserving the amorphous state up to 800 °C. When crystallization occurs at higher processing temperatures, it leads to the formation of tailored multiphase glass-ceramics containing pseudowollastonite and wollastonite. This structural adaptability provides a direct mechanism to modulate the material's performance: lower sintering temperatures maximize surface reactivity and accelerate early-stage HAp deposition, whereas higher temperatures significantly enhance Vickers hardness and Young's modulus through densification and controlled crystallization, while still ensuring long-term bioactivity. In conclusion, the ability to regulate the simultaneous, controlled release of therapeutic silicon, magnesium, and strontium ions, coupled with reproducible structural and mechanical properties, suggests that SPS-processed Bio_MS represents a highly adaptable and innovative approach for advanced bone tissue engineering applications.

CRediT authorship contribution statement

Martina Tetti: Writing – original draft, Validation, Methodology, Investigation. **Roberto Orrù:** Writing – review & editing, Writing – original draft, Validation, Supervision, Methodology, Investigation, Data curation, Conceptualization. **Giacomo Cao:** Writing – review & editing, Supervision, Conceptualization. **Sebastiano Garroni:** Writing – review & editing, Methodology, Investigation, Data curation. **Simone De Micco:** Methodology, Investigation, Data curation. **Devis Bellucci:** Writing – review & editing, Writing – original draft, Validation, Supervision, Methodology, Investigation, Data curation, Conceptualization. **Valeria Cannillo:** Writing – review & editing, Writing – original draft, Validation, Supervision, Methodology, Investigation, Data curation, Conceptualization.

Declaration of Competing Interest

The authors declare that they have no known competing financial interests or personal relationships that could have appeared to influence the work reported in this paper.

Acknowledgements

Martina Tetti performed her activity in the framework of the International PhD in Innovation Sciences and Technologies at the University of Cagliari, Italy. The authors acknowledge the Polilab of the University of Cagliari for the use of the Bruker D8 Advance diffractometer.

Appendix A. Supporting information

Supplementary data associated with this article can be found in the online version at doi:10.1016/j.jeurceramsoc.2026.118945.

References

[1] L.L. Hench, The story of Bioglass®, J. Mater. Sci. Mater. Med. 17 (2006) 967–978, https://doi.org/10.1007/s10856-006-0432-z.
[2] L.C. Gerhardt, A.R. Boccaccini, Bioactive glass and glass-ceramic scaffolds for bone tissue engineering, Materials 3 (2010) 3867, https://doi.org/10.3390/ma3073867.
[3] M.N. Rahaman, D.E. Day, B. Sonny Bal, Q. Fu, S.B. Jung, L.F. Bonewald, A. P. Tomsia, Bioactive glass in tissue engineering, Acta Biomater. 7 (6) (2011) 2355–2373, https://doi.org/10.1016/j.actbio.2011.03.016.
[4] J.R. Jones, Review of bioactive glass: from Hench to hybrids, Acta Biomater. 9 (2013) 4457–4486, https://doi.org/10.1016/j.actbio.2012.08.023.
[5] H. Madival, A. Rajiv, A comprehensive review of bioactive glasses: synthesis, characterization, and applications in regenerative medicine, Biomed. Mater. Devices 4 (2026) 1380–1400, https://doi.org/10.1007/s44174-025-00310-8.
[6] F. Baino, S. Yamaguchi, The use of simulated body fluid (SBF) for assessing materials bioactivity in the context of tissue engineering: Review and challenges, Biomimetics 5 (2020) 1–19, https://doi.org/10.3390/biomimetics5040057.
[7] A. Hoppe, V. Mourino, A.R. Boccaccini, Therapeutic inorganic ions in bioactive glasses to enhance bone formation and beyond, Biomater. Sci. 1 (3) (2013) 254–256, https://doi.org/10.1039/C2BM00116K.
[8] A. Moghanian, L. Dehghan Mehrjardi, S. Safaee, Ion substitution in bioactive glass: A comprehensive review of structural modifications and functional effects, Materials 8 (2025) 100598, https://doi.org/10.1016/j.nxmate.2025.100598.
[9] L. Lefebvre, J. Chevalier, L. Gremillard, R. Zenati, G. Thollet, D. Bernache-Assolant, A. Govin, Structural transformations of bioactive glass 45S5 with thermal treatments, Acta Mater. 55 (10) (2007) 3305–3313, https://doi.org/10.1016/j.actamat.2007.01.029.
[10] A. Pedone, V. Cannillo, M.C. Menziani, Toward the understanding of crystallization, mechanical properties and reactivity of multicomponent bioactive glasses, Acta Mater. 213 (2021) 116977, https://doi.org/10.1016/j.actamat.2021.116977.
[11] Z. Jia, J. Zhang, C. Jia, J. Nie, K. Chu, Preparation and characterization of mechanical properties of carbon nanotube/45S5Bioglass composites for biologic applications, Mater. Sci. Eng. A 528 (3) (2011) 1553–1557, https://doi.org/10.1016/j.msea.2010.10.077.
[12] Q.Z. Chen, J.L. Xu, L.G. Yu, X.Y. Fang, K.A. Khor, Spark plasma sintering of sol-gel derived 45S5 Bioglass®-ceramics: Mechanical properties and biocompatibility evaluation, Mater. Sci. Eng. C. 32 (3) (2012) 494–502, https://doi.org/10.1016/j.msec.2011.11.023.
[13] S. Grasso, R.K. Chinnam, H. Porwal, A.R. Boccaccini, M.J. Reece, Low temperature spark plasma sintering of 45S5 Bioglass®, J. Non-Cryst. Solids 362 (1) (2013) 25–29, https://doi.org/10.1016/j.jnoncrysol.2012.11.009.
[14] L. Desogus, A. Cuccu, S. Montinaro, R. Orrù, G. Cao, D. Bellucci, A. Sola, V. Cannillo, Classical Bioglass® and innovative CaO-rich bioglass powders processed by Spark Plasma Sintering: A comparative study, J. Eur. Ceram. Soc. 35 (15) (2015) 4277–4285, https://doi.org/10.1016/j.jeurceramsoc.2015.07.023.
[15] Z. Li, B.C. Thompson, H. Hu, K.A. Khor, Rapid fabrication of dense 45S5 Bioglass® compacts through spark plasma sintering and evaluation of their in vitro biological properties, Biomed. Mater. (Bristol U. K.) 11 (6) (2016) 065006, https://doi.org/10.1088/1748-6041/11/6/065006.
[16] L. Bertolla, I. Dlouhy, P. Tatarko, A. Viani, A. Mahajan, Z. Chlup, M.J. Reece, A. R. Boccaccini, Pressureless spark plasma–sintered Bioglass® 45S5 with enhanced mechanical properties and stress–induced new phase formation, J. Eur. Ceram. Soc. 37 (7) (2017) 2727–2736, https://doi.org/10.1016/j.jeurceramsoc.2017.02.003.
[17] Z. Li, N.W. Khun, X.-Z. Tang, E. Liu, K.A. Khor, Mechanical, tribological and biological properties of novel 45S5 Bioglass® composites reinforced with in situ reduced graphene oxide, J. Mech. Behav. Biomed. Mater. 65 (2017) 77–89, https://doi.org/10.1016/j.jmbbm.2016.08.007.
[18] D. Angioni, R. Orrù, G. Cao, S. Garroni, A. Iacomini, D. Bellucci, V. Cannillo, Spark plasma sintering, mechanical and in-vitro behavior of a novel Sr- and Mg-containing bioactive glass for biomedical applications, J. Eur. Cer. Soc. 42 (4) (2022) 1776–1783, https://doi.org/10.1016/j.jeurceramsoc.2021.11.061.
[19] A. Gharbi, S. Ayadi, N. Jouini, F. Schoenstein, H. Oudadess, H.E. Feki, W. Cheikhrouhou-Koubaa, Original implementation of low-temperature SPS for bioactive glass used as a bone biomaterial, J. Mech. Behav. Biomed. Mater. 126 (2022) 104988, https://doi.org/10.1016/j.jmbbm.2021.104988.
[20] M. Khoeini, S. Hesaraki, A. Kolahi, The sintering behavior, in vitro performance, and radiopacity of spark plasma sintered barium-containing calcium-phospho-alumino-borosilicate glass powders, Ceram. Int. 48 (20) (2022) 30704–30716, https://doi.org/10.1016/j.ceramint.2022.07.019.
[21] M. Manohar, K. Balani, Association of Non-Bridging Oxygen with Cytocompatibility in Cerium and Cobalt Codoped 58S Bioglass, ACS Biomater. Sci. Eng. 12 (3) (2026) 1474–1491, https://doi.org/10.1021/acsbiomaterials.5c01523.
[22] D. Bellucci, V. Cannillo, G. Ciardelli, P. Gentile, A. Sola, Potassium based bioactive glass for bone tissue engineering, Ceram. Int. 36 (2010) 2449–2453, https://doi.org/10.1016/j.ceramint.2010.07.009.
[23] D. Bellucci, V. Cannillo, A. Sola, Calcium and potassium addition to facilitate the sintering of bioactive glasses, Mater. Lett. 65 (2011) 1825–1827, https://doi.org/10.1016/j.matlet.2011.03.060.
[24] D. Bellucci, A. Sola, V. Cannillo, Low temperature sintering of innovative bioactive glasses, J. Am. Ceram. Soc. 95 (2012) 1313–1319, https://doi.org/10.1111/j.1551-2916.2012.05100.x.
[25] D. Bellucci, V. Cannillo, A novel bioactive glass containing strontium and magnesium with ultra-high crystallization temperature, Mater. Lett. 213 (2018) 67–70, https://doi.org/10.1016/j.matlet.2017.11.020.
[26] D. Bellucci, E. Veronesi, M. Dominici, V. Cannillo, A new bioactive glass with extremely high crystallization temperature and outstanding biological performance, Mater. Sci. Eng. C. 110 (2020) 110699, https://doi.org/10.1016/j.msec.2020.110699.
[27] M. Diba, F. Tapia, A.R. Boccaccini, L.A. Strobel, Magnesium-containing bioactive glasses for biomedical applications, Int. J. Appl. Glass Sci. 3 (2012) 221–253, https://doi.org/10.1111/j.2041-1294.2012.00095.x.
[28] I. Cacciotti, Bivalent cationic ions doped bioactive glasses: the influence of magnesium, zinc, strontium and copper on the physical and biological properties, J. Mater. Sci. 52 (2017) 8812–8831, https://doi.org/10.1007/s10853-017-1010-0.
[29] J. Lao, J.-M. Nedelec, E. Jallot, New strontium-based bioactive glasses: physicochemical reactivity and delivering capability of biologically active dissolution products, J. Mater. Chem. 19 (2009) 2940–2949, https://doi.org/10.1039/B822214B.
[30] J. Isaac, J. Nohra, J. Lao, E. Jallot, Effects of Strontium-Doped Bioactive Glass on the Differentiation of Cultured Osteogenic Cells, Eur. Cell. Mater. 21 (2014) 130–143, https://doi.org/10.22203/ecm.v021a11.

[31] H.B. Pan, X.L. Zhao, X. Zhang, K.B. Zhang, L.C. Li, Z.Y. Li, W.M. Lam, W.W. Lu, D. P. Wang, W.H. Huang, K.L. Lin, J. Chang, Strontium borate glass: potential biomaterial for bone regeneration, J. R. Soc. Interface 7 (48) (2010) 1025–1031, https://doi.org/10.1098/rsif.2009.0504.
[32] A. Anesi, M. Ferretti, R. Salvatori, D. Bellucci, F. Cavani, M. Di Bartolomeo, C. Palumbo, V. Cannillo, *In-vivo* evaluations of bone regenerative potential of two novel bioactive glasses, J. Biomed. Mater. Res. A 111 (2023) 1264–1278, https://doi.org/10.1002/jbm.a.37526.
[33] M. Barbalinardo, M. Ferretti, V. Stanzani, F. Chiarini, I. Zanoni, F. Paganelli, M. Checchi, S. Truocchio, M. Corradini, V.R. Lo Vasco, F. Cavani, L. Reggiani Bonetti, D. Bellucci, V. Cannillo, C. Palumbo, Magnesium and Strontium-Enriched Bioactive Glasses: Superior Biocompatibility and Angiogenesis, beyond the gold standard, Biomater. Adv. 177 (2025) 214379, https://doi.org/10.1016/j.bioadv.2025.214379.
[34] D. Angioni, R. Orrù, G. Cao, S. Garroni, D. Bellucci, V. Cannillo, Recent advances on innovative bioactive glass-hydroxyapatite composites for bone tissue applications: Processing, mechanical properties, and biological performance, J. Eur. Ceram. Soc. 43 (2023) 7688–7696, https://doi.org/10.1016/j.jeurceramsoc.2023.07.079.
[35] L. Lutterotti, R. Ceccato, R. Dal Maschio, E. Pagani, Quantitative analysis of silicate glass in ceramic materials by the Rietveld method, Mater. Sci. Forum 278-281 (1998) 87, https://doi.org/10.4028/www.scientific.net/MSF.278-281.87.
[36] M. Baricco, T.A. Baser, S. Enzo, G. Vaughan, A.R. Yavari, Analysis of crystallization behavior of Fe48Cr15Mo14Y2C15B6 bulk metallic glass by synchrotron radiation, J. Mater. Res. 23 (2008) 2166–2173, https://doi.org/10.1557/JMR.2008.0264.
[37] J. Massera, S. Fagerlund, L. Hupa, M. Hupa, Crystallization mechanism of the bioactive glasses, 45S5 and S53P4, J. Am. Ceram. Soc. 95 (2) (2012) 607–613, https://doi.org/10.1111/j.1551-2916.2011.05012.x.
[38] W.C. Oliver, G.M. Pharr, An Improved Technique for Determining Hardness and Elastic Modulus Using Load and Displacement Sensing Indentation Experiments, J. Mater. Res. 7 (1992) 1564–1583, https://doi.org/10.1557/JMR.1992.1564.
[39] T. Kokubo, H. Takadama, How useful is SBF in predicting in vivo bone bioactivity? Biomaterials 27 (15) (2006) 2907–2915, https://doi.org/10.1016/j.biomaterials.2006.01.017.
[40] K. Matusita, S. Sakka, Kinetic study of crystallization of glass by differential thermal analysis-criterion on application of Kissinger plot, J. Non-Cryst. Solids 38-39 (1980) 741–746, https://doi.org/10.1016/0022-3093(80)90525-6.
[41] A. Baranowska, M. Leśniak, M. Kochanowicz, J. Żmojda, P. Miluski, D. Dorosz, Crystallization Kinetics and Structural Properties of the 45S5 Bioactive Glass and Glass-Ceramic Fiber Doped with Eu^{3+}, Materials 13 (2020) 1281, https://doi.org/10.3390/ma13061281.
[42] K.E. Wallace, R.G. Hill, J.T. Pembroke, et al., Influence of sodium oxide content on bioactive glass properties, J. Mater. Sci. Mater. Med. 10 (1999) 697–701, https://doi.org/10.1023/A:1008910718446.
[43] J. Massera, L. Hupa, M. Hupa, Influence of the partial substitution of CaO with MgO on the thermal properties and in vitro reactivity of the bioactive glass S53P4, J. Non-Cryst. Solids 358 (18–19) (2012) 2701–2707, https://doi.org/10.1016/j.jnoncrysol.2012.06.032.
[44] A. Al-Noaman, S.C.F. Rawlinson, R.G. Hill, The role of MgO on thermal properties, structure and bioactivity of bioactive glass coating for dental implants, J. Non-Cryst. Solids 358 (22) (2012) 3019–3027, https://doi.org/10.1016/j.jnoncrysol.2012.07.039.
[45] J.D. Salazar-Martinez, P.A. Forero-Sossa, J. Henao, A.L. Giraldo-Betancur, SrO-Containing Bioactive Glasses in the SiO_2–CaO–P_2O_5 System: A Comprehensive Review, ACS Biomater. Sci. Eng. 11 (12) (2025) 6997–7030, https://doi.org/10.1021/acsbiomaterials.5c01097.
[46] S.M. Rabiee, N. Nazparvar, M. Azizian, D. Vashaee, L. Tayebi, Effect of ion substitution on properties of bioactive glasses: A review, Ceram. Int. 41 (6) (2015) 7241–7251, https://doi.org/10.1016/j.ceramint.2015.02.140.
[47] F.J. Hmood, O. Goerke, F. Schmidt, J. Dirk E, J. Günster, Structure and crystallization characterization of chemically developed bioactive glass based on ICIE16, Open. Ceram. 3 (2020) 100027, https://doi.org/10.1016/j.oceram.2020.100027.
[48] M. Luginina, D. Angioni, S. Montinaro, R. Orrù, G. Cao, R. Sergi, D. Bellucci, V. Cannillo, Hydroxyapatite/bioactive glass functionally graded materials (FGM) for bone tissue engineering, J. Eur. Ceram. Soc. 40 (2020) 4623–4634, https://doi.org/10.1016/j.jeurceramsoc.2020.05.061.
[49] A.R. Franco Jr., G. Pintaúde, A. Sinatora, C.E. Pinedo, A.P. Tschiptschin, The Use of a Vickers Indenter in Depth Sensing Indentation for Measuring Elastic Modulus and Vickers Hardness, Mater. Res. 7 (3) (2004) 483–491, https://doi.org/10.1590/S1516-14392004000300018.
[50] F.G. Mecca, D. Bellucci, V. Cannillo, Effect of Thermal Treatments and Ion Substitution on Sintering and Crystallization of Bioactive Glasses: A Review, Materials 16 (2023) 4651, https://doi.org/10.3390/ma16134651.
[51] F. Sharifianjazi, M. Moradi, A. Abouchenari, A.H. Paksereshtt, A. Esmaeilkhanian, M. Shokouhimehr, M. Shahedi, Asl Effects of Sr and Mg dopants on biological and mechanical properties of SiO_2–CaO–P_2O_5 bioactive glass, Ceram. Int. 46 (14) (2020) 22674–22682, https://doi.org/10.1016/j.ceramint.2020.06.030.
[52] Z.W. Loh, M.H.M. Zaid, K.A. Matori, M.M.A. Kechik, Y.W. Fen, M.Z.H. Mayzan, S. Liza, W.M. Cheong, Phase transformation and mechanical properties of new bioactive glass-ceramics derived from CaO–P_2O_5–Na_2O–B_2O_3–SiO_2 glass system, J. Mech. Behav. Biomed. Mater. 143 (2023) 105889, https://doi.org/10.1016/j.jmbbm.2023.105889.
[53] A. Dridi, K.Z. Riahi, S. Somrani, Mechanism of apatite formation on a poorly crystallized calcium phosphate in a simulated body fluid (SBF) at 37 °C, J. Phys. Chem. Solids 156 (2021) 110122, https://doi.org/10.1016/j.jpcs.2021.110122.
[54] F. Baino, G. Novajra, V. Miguez-Pacheco, A.R. Boccaccini, C. Vitale-Brovarone, Bioactive glasses: Special applications outside the skeletal system, J. Non-Cryst. Solids 432 (2016) 15–30, https://doi.org/10.1016/j.jnoncrysol.2015.02.015.
[55] E.C. Ziemath, M.A. Aegerter, Raman and infrared investigations of glass and glass-ceramics with composition $2Na_2O{\cdot}1CaO{\cdot}3SiO_2$, J. Mater. Res. 9 (1994) 216–225, https://doi.org/10.1557/JMR.1994.0216.
[56] P. Gonzalez, J. Serra, S. Liste, S. Chiussi, B. Leon, M. Perez-Amor, Raman spectroscopic study of bioactive silica based glasses, J. Non-Cryst. Solids 320 (2003) 92–99, https://doi.org/10.1016/S0022-3093(03)00013-9.
[57] A. Antonakos, E. Liarokapis, T. Leventouri, Micro-Raman and FTIR studies of synthetic and natural apatites, Biomaterials 28 (19) (2007) 3043–3054, https://doi.org/10.1016/j.biomaterials.2007.02.028.
[58] A. Awonusi, M.D. Morris, M.M.J. Tecklenburg, Carbonate Assignment and Calibration in the Raman Spectrum of Apatite, Calcif. Tissue Int. 81 (2007) 46–52, https://doi.org/10.1007/s00223-007-9034-0.
[59] G. Penel, G. Leroy, C. Rey, E. Bres, MicroRaman, Spectral Study of the PO4 and CO3 Vibrational Modes in Synthetic and Biological Apatites, Calcif. Tissue Int. 63 (1998) 475–481, https://doi.org/10.1007/s002239900561.
[60] E. Dietrich, H. Oudadesse, A. Lucas-Girot, M. Mami, vitro bioactivity of melt-derived glass 46S6 doped with magnesium, J. Biomed. Mater. Res. 88A (2009) 1087–1096, https://doi.org/10.1002/jbm.a.31901.
[61] A. Moghanian, H.J. Haugen, D. Marović, From atomic scale to biological performance: the role of magnesium in solubility of the network and bioactivity of 45S5 Bioglass®, J. Non-Cryst. Solids 680 (2026) 124046 https://doi.org/10.1016/j.jnoncrysol.2026.124046.
[62] Y.C. Fredholm, N. Karpukhina, D.S. Brauer, J.R. Jones, R.V. Law, R.G. Hill, Influence of strontium for calcium substitution in bioactive glasses on degradation, ion release and apatite formation, J. R. Soc. Interface 9 (70) (2012) 880–889, https://doi.org/10.1098/rsif.2011.0387.
[63] A. Hamdan, A. Hajimohammadi, A. Rawal, T. Kim, The intrinsic role of network modifiers (Ca versus Mg) in the reaction kinetics and microstructure of sodium silicate-activated CaO-MgO-Al_2O_3-SiO_2 glasses, Cem. Concr. Res. 164 (2023) 107058, https://doi.org/10.1016/j.cemconres.2022.107058.
[64] R. Wetzel, O. Bartzok, D.S. Brauer, Influence of low amounts of zinc or magnesium substitution on ion release and apatite formation of Bioglass 45S5, J. Mater. Sci Mater. Med. 31 (2020) 86, https://doi.org/10.1007/s10856-020-06426-1.